Available online at www.sciencedirect.com

SCIENCE DIRECT®

International Journal of Heat and Mass Transfer 48 (2005) 1330–1349

International Journal of HEAT and MASS TRANSFER

www.elsevier.com/locate/ijhmt

Heat transfer to flow through porous passages using extended weighted residuals method—a Green's function solution

A. Haji-Sheikh [a,*], E.M. Sparrow [b], W.J. Minkowycz [c]

[a] *Department of Mechanical and Aerospace Engineering, The University of Texas at Arlington, 500 West First Street, Arlington, TX 76019-0023, United States*

[b] *Department of Mechanical Engineering, University of Minnesota, Minneapolis, MN 55455-0111, United States*

[c] *Department of Mechanical and Industrial Engineering, University of Illinois at Chicago, Chicago, IL 60607-7022, United States*

Received 1 August 2004; received in revised form 1 October 2004
Available online 10 December 2004

Abstract

The Green's function solution method is a direct and powerful tool for solving heat transfer problems associated with flow through passages. It is also an equally powerful tool when these passages are filled with saturated porous materials. The capability of the Green's function solution is enhanced when it is used in conjunction with the method of weighted residuals extended for this type of application. This study discusses the calculation of heat transfer to fluids flowing through different porous passages by using this combined methodology. The numerical illustrations include the study of heat transfer in isosceles triangular passages. Also, this methodology is equally applicable when the boundary conditions are of the first, second, or third kind.

1. Introduction

Variational calculus has been used in the past to study various heat transfer problems. An early use of variational calculus by Sparrow and Seigel [1] concerns a determination of the heat transfer to fluid flow in rectangular ducts. Later, the finite element method has evolved also based on variational calculus. Moreover, the method of weighted residuals, often called the Galerkin method [2], is also based on variational calculus. The Galerkin method has been often used to solve the Poison's equation. The method of weighted residuals was extended for solving the eigenvalues problems in [3]. This study discusses the Green's function solution for flow through porous passages. A Green's function solution, based on variational calculus, is a powerful tool to study heat transfer in passages saturated with porous materials.

In porous media applications, the study of heat transfer in elliptical passages, using an extended weighted residuals (EWR) method is in [4]. It reports the local and average heat transfer coefficient due to a step change in the temperature at the walls. The utilization of the Green's function solution enables one to extend the procedure to include the effect of frictional heating, variable wall temperature, etc. [5].

The studies of heat transfer in the thermal entrance region, in the presence of frictional heating and axial conduction, are in Nield et al. [6] for parallel-plate channels and in Kuznetsov et al. [7] for circular pipes; they studied different forms of frictional heating. This study

* Corresponding author. Tel.: +1 817 272 2010; fax: +1 817 272 2952.

E-mail address: haji@mae.uta.edu (A. Haji-Sheikh).

doi:10.1016/j.ijheatmasstransfer.2004.10.002

Nomenclature

A	area, m^2
$\mathbf{A}$	matrix
a_{ij}	elements of matrix $\mathbf{A}$
$\mathbf{B}$	matrix
b_{ij}	elements of matrix $\mathbf{B}$
B_m	coefficient
C	duct contour, m
c_p	specific heat, J/kg K
$\mathbf{D}$	matrix
Da	Darcy number, K/L_c^2
D_h	hydraulic diameter $4A/C$, m
d_{mj}	coefficient
d_{mj}	elements of matrix $\mathbf{D}$
$\mathbf{E}$	matrix with elements e_{ij}
Ec	Eckert number, $U^2/c_p\Delta T$
e_{ij}	elements of matrix $\mathbf{E}$
f_i, f_j	basis functions
h	heat transfer coefficient, $W/m^2 K$
I	minimization function
H	triangle dimension in Fig. 1(b)
$\bar{h}$	average heat transfer coefficient $W/m^2 K$
G	Green's function
i,j	indices
K	permeability, m^2
k_e	effective thermal conductivity, W/m K
L_c	characteristic length, m
M	μ_e/μ
N	matrix dimension
Nu_D	Nusselt number, hD_h/k
m,n	indices
$\vec{n}$	normal to surface
$\mathbf{P}$	matrix having elements p_{mi}
Pe	Peclet number, $\rho c_p L_c U/k$
p	pressure, Pa
p_{mi}	elements of matrix $\mathbf{P}$
Re_D	Reynolds number, $\rho U D_h/\mu_e$

r	radial coordinate, m
r_0	pipe radius, m
S	volumetric heat source, W/m^3
S^*	frictional heating effect, Eq. (27b)
T	temperature, K
T_i	temperature at $x = 0$, K
U	average velocity, m/s
$\overline{U}$	average value of $\bar{u}$
u	velocity, m/s
$\bar{u}$	$\bar{u} = \mu u/(\Phi L_c^2)$
W	dimension in Fig. 1(b)
x	axial coordinate, m
$\bar{x}$	$x/(PeH)$ or $\bar{x} = x/(Per_0)$
y, z	coordinates, m
Greek symbols	
δ_j	velocity coefficient
η_j	basis functions for velocity
θ	$(T - T_w/T_i - T_w)$
λ_m	eigenvalues
μ	fluid viscosity, N s/m^2
μ_e	effective viscosity, N s/m^2
ξ	dimensionless coordinate,
ρ	density, kg/m^3
Φ	$-\partial p/\partial x$
ϕ	half apex angle
ψ	eigenfunction
Ω	pressure vector with element ω_i
ω_i	element of vector Ω
Subscripts	
B	bulk
i	inlet condition
S	source effect
W	wall or wall effect
w	wall

uses the modified form of the frictional heating effect discussed in Al-Hadhrami et al. [8]. The studies related to the thermally developing forced convection with constant wall heat flux in parallel-plate channels and circular pipes are reported by Nield et al. [9]. General information related to flow in porous passages is in [10–12].

This paper discusses the combined effects of two powerful mathematical procedures when applied to the problems associated with flow through porous passages. The Green's function solution permits one to directly include thermal conditions at the wall, volumetric heat sources that include frictional heating, and inlet temperature distribution. The classical Green's function, in [5], applies to regular geometries when the separation of spatial variables is possible. The EWR method is a unified solution technique that can be used for regular geometries such as circular pipes, as well as, irregular geometries such as triangular passages. Additionally, the method of weighted residual simplifies the computation of the Green's function. Of course this methodology only applies to a system of linear partial differential equations.

2. The working relations

Although the working relations are widely available in the literature, their appearance in this paper is for the convenience of identification of the working parameters in subsequent numerical analysis. Therefore, a brief presentation of these relations is to appear a priori.

2.1. Governing momentum equation

For a fluid passage with a constant but arbitrarily shaped cross-section as shown in Fig. 1(a), the Brinkman momentum equation,

$$\mu_e\left(\frac{\partial^2 u}{\partial y^2}+\frac{\partial^2 u}{\partial z^2}\right)-\frac{\mu}{K}u-\frac{\partial p}{\partial x}=0 \tag{1}$$

leads toward the computation of a fully developed velocity profile in which the pressure gradient $\Phi = -\partial p/\partial x$ is a constant. The dimensionless form of Eq. (1) is

$$M\left(\frac{\partial^2 \bar{u}}{\partial \bar{y}^2}+\frac{\partial^2 \bar{u}}{\partial \bar{z}^2}\right)-\frac{1}{Da}\bar{u}-1=0 \tag{2}$$

wherein $\bar{y} = y/L_c$, $\bar{z} = z/L_c$ $M = \mu_e/\mu$, $\bar{u} = \mu u/(\Phi L_c^2)$, and $Da = K/L_c^2$ is the Darcy number. Moreover, μ_e is the effective viscosity, μ is the fluid viscosity, K the permeability, and L_c is arbitrarily chosen as the characteristic length. The solution of Eq. (2), with the boundary condition $\bar{u} = 0$ at the wall, is often obtainable using the variational calculus and, by definition, the mean velocity is

$$U=\frac{1}{A}\int_A u\,\mathrm{d}A. \tag{3}$$

2.2. Governing energy equation

Under steady-state condition and when thermophysical properties are independent of temperature, the energy equation for fully developed and incompressible flow is

$$\rho c_p u\frac{\partial T}{\partial x}=\frac{\partial}{\partial x}\left(k_e\frac{\partial T}{\partial x}\right)+\frac{\partial}{\partial y}\left(k_e\frac{\partial T}{\partial y}\right)+\frac{\partial}{\partial z}\left(k_e\frac{\partial T}{\partial z}\right)+S(x,y,z), \tag{4}$$

where volumetric heat source $S(x, y, z)$ represents the contribution of frictional heating. The parameters ρc_p and k_e are the equivalent thermal capacitance and the thermal conductivity, respectively. In the following mathematical formulations, the parameters ρc_p and k_e may depend on y and z but remain independent of x. Moreover, in this presentation, the contribution of axial conduction deferred to the subsequent publications. Accordingly, for convenience of mathematical formulations, Eq. (4) reduces to

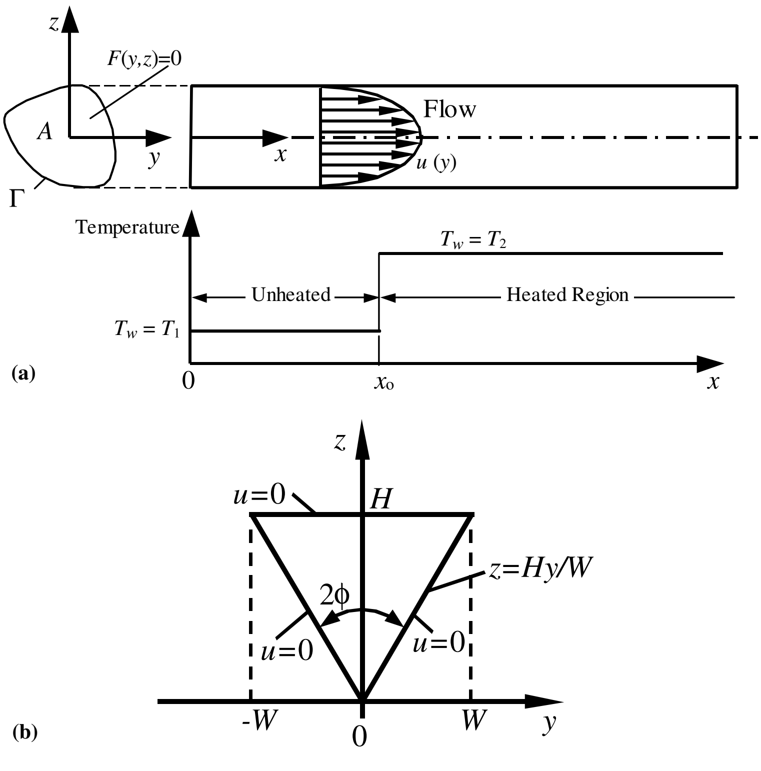

Fig. 1. Schematics of porous passages: (a) selected coordinates and boundary conditions and (b) isosceles triangular passages, geometry and dimensions.

$$\frac{\partial}{\partial y}\left(k_e\frac{\partial T}{\partial y}\right)+\frac{\partial}{\partial z}\left(k_e\frac{\partial T}{\partial z}\right)+S(y,z;x)=\rho c_p u\frac{\partial T}{\partial x}. \quad (5)$$

The solutions for Eqs. (2) and (5) appear later following a brief presentation of a methodology that uses the variational calculus.

3. Application of variational calculus

The emphasis of this analysis is to compute the Green's function in order to utilize the Green's function solution. For the purpose of the computation of the Green's function, Eq. (5), without the source term, is of current interest. Because, once the Green's function is known, the Green's function solution will provide the contribution of any source term. A preliminary step is to separate the axial variable in Eq. (5) and then the temperature solution takes the following form,

$$T(y,z;x)=\Psi(y,z)e^{-\lambda^2 x}. \quad (6)$$

In the absence of the source term, the substitution of $T(y,z;x)$ from Eq. (6) in Eq. (5) yields the relation

$$\frac{\partial}{\partial y}\left(k_e\frac{\partial \Psi}{\partial y}\right)+\frac{\partial}{\partial z}\left(k_e\frac{\partial \Psi}{\partial z}\right)+\lambda^2\rho c_p u\Psi=0. \quad (7)$$

In general, Eqs. (1) and (7) have similar forms and both solutions are obtainable via a similar methodology. The primary attention is directed toward the solution of Eq. (7) subject to boundary conditions of the first, second kind, or third kind. The variational calculus procedure in [1,2] is modified and used to minimize the following functional relation

$$I=\int_A\left\{k_e\left(\frac{\partial\Psi}{\partial y}\right)^2+k_e\left(\frac{\partial\Psi}{\partial z}\right)^2-\lambda^2\rho c_p u\Psi^2 -\frac{1}{2}\left[\frac{\partial}{\partial y}\left(k_e\frac{\partial\Psi^2}{\partial y}\right)+\frac{\partial}{\partial z}\left(k_e\frac{\partial\Psi^2}{\partial z}\right)\right]\right\}dA, \quad (8)$$

where A is the cross-section area. Next, consider the solution for function Ψ to have the form

$$\Psi=\sum_{j=1}^{N}d_j f_j(y,z). \quad (9)$$

A complete and linearly independent set of functions $f_j(y,z)$, for $j=1,2,\ldots,N$, is known as the basis functions and their method of selection is to appear later.

Following the substitution of Ψ from Eq. (9) in Eq. (8), the minimization of functional $I(d_1,d_2,\ldots,d_N)$ requires having

$$\frac{\partial I}{\partial d_i}=0,\quad \text{for } i=1,2,\ldots,N \quad (10)$$

and d_i is any one of the coefficients in Eq. (9). The differentiation of I in Eq. (8), with respect to d_j, leads toward the relation

$$\frac{\partial I}{\partial d_i}=2\int_A\left[k_e\left(\frac{\partial\Psi}{\partial y}\right)\frac{\partial f_i}{\partial y}+k_e\left(\frac{\partial\Psi}{\partial z}\right)\frac{\partial f_i}{\partial y}-\lambda^2\rho c_p u\Psi f_i\right]dA -\int_A\left[\frac{\partial}{\partial y}\left(k_e\frac{\partial(\Psi f_i)}{\partial y}\right)+\frac{\partial}{\partial y}\left(k_e\frac{\partial(\Psi f_i)}{\partial z}\right)\right]dA=0$$
$$\text{for } i=1,2,\ldots,N. \quad (11)$$

Note that, the first two terms within the first square brackets have the form

$$k_e\nabla\Psi\cdot\nabla f_i=\nabla\cdot[f_i(k_e\nabla\Psi)]-\nabla\cdot(k_e\nabla\Psi)f_i$$

and, therefore, Eq. (11) takes the following form,

$$2\int_A\left[\frac{\partial}{\partial y}\left(k_e\frac{\partial\Psi}{\partial y}\right)+\frac{\partial}{\partial y}\left(k_e\frac{\partial\Psi}{\partial z}\right)+\lambda^2\rho c_p u\Psi\right]f_i\,dA -2\int_A\nabla\cdot[f_i(k_e\nabla\Psi)]\,dA+\int_A\nabla\cdot[k_e\nabla(\Psi f_i)]\,dA=0. \quad (12)$$

Using the divergence theorem, the second integral in Eq. (12) becomes

$$-2\int_A\nabla\cdot[f_i(k_e\nabla\Psi)]\,dA=-2\int_\Gamma f_i(k_e\nabla\Psi)\cdot\vec{n}\,ds =-2\int_\Gamma f_i k_e\frac{\partial\Psi}{\partial n}\,ds. \quad (13a)$$

Similarly, using the divergence theorem, the third integral in Eq. (12) becomes

$$\int_A\nabla\cdot[k_e\nabla(\Psi f_i)]\,dA=\int_\Gamma k_e\frac{\partial(\Psi f_i)}{\partial n}\,ds =\int_\Gamma k_e\left(f_i\frac{\partial\Psi}{\partial n}+\Psi\frac{\partial f_i}{\partial n}\right)ds. \quad (13b)$$

It is necessary for this boundary integral to vanish on the boundary Γ. Accordingly, the functions $f_i(y,z)$ should satisfy the conditions $f_i(y_c,z_c)=0$ for the boundary conditions of the first kind and that makes the right side of Eq. (13a) and Eq. (13b) vanish. For the boundary conditions of the second kind, the selection of functions $\partial f_i(y_c,z_c)/\partial n=0$ make $\partial\Psi/\partial n=0$ because of Eq. (9). For the boundary condition of the third kind, $k_e\partial f_i/\partial n=-hf_i$ and $k_e\partial\Psi/\partial n=-h\Psi$, where h is a constant coefficient; this makes the magnitudes of the right sides in Eq. (13a) and Eq. (13b) to become

$$2\int_\Gamma hf_i\Psi\,ds,$$

the same for each f_i but with different signs.

Finally, when the basis functions f_j, in Eq. (9), are selected to satisfy a boundary condition of the first, second, or third kind, Eq. (12) reduces to the relation,

$$\sum_{j=1}^{N}d_j\left\{\int_A\left[\frac{\partial}{\partial y}\left(k_e\frac{\partial f_j(y,z)}{\partial y}\right)+\frac{\partial}{\partial y}\left(k_e\frac{\partial f_j(y,z)}{\partial z}\right)\right]f_i\,dA +\lambda^2\int_A\rho c_p u f_j f_i\right\}=0,\quad \text{for } i=1,2,\ldots,N. \quad (14)$$

Eq. (14) represents a system of N equations for $N+1$ unknowns that include the value of λ^2. In the matrix form, Eq. (14) assumes the following form

$$(\mathbf{A} + \lambda^2\mathbf{B}) \cdot \mathbf{d} = 0, \tag{15}$$

wherein the matrices **A** and **B** have the members

$$a_{ij} = \int_A f_i(\mathbf{y}, z)\nabla \cdot [k_e \nabla f_j(\mathbf{y}, z)]\,\mathrm{d}A$$
$$= -\int_A k_e \nabla f_i(\mathbf{y}, z) \cdot \nabla f_j(\mathbf{y}, z)\,\mathrm{d}A \tag{16a}$$

and

$$b_{ij} = \int_A \rho c_p u(y, z) f_i(y, z) f_j(y, z)\,\mathrm{d}A \tag{16b}$$

and the matrices **A** and **B** are symmetric [3]. In this formulation, the parameters k_e and ρc_p may have constant values or depend on coordinates y and z. The unknown coefficients $(d_1, d_2, \ldots, d_N)$ are the members of vector **d**. Because **A** and **B** are symmetric, these coefficients and the eigenvalues are obtainable from Eq. (15) following the application of the Colesky decomposition technique [3]. An alternative and simple procedure is to have an alternative form of Eq. (15), that is

$$(\mathbf{B}^{-1}\mathbf{A} + \lambda^2\mathbf{I})\mathbf{d} = 0 \tag{17}$$

a standard eigenvalue problem whose N eigenvalues can be determined by various numerical techniques.

The aforementioned formulation provides a unique capability. This procedure equally applies to passages of different cross-section profiles. They include passages with regular boundaries such as circular passages and passages with non-orthogonal boundaries such as triangular, trapezoidal, and other similar profiles. For any duct, the functions $f_j(y,z)$ are to be selected so that they satisfy the homogeneous boundary conditions along the surface of the ducts. Next, Eq. (17) can provide N eigenvalues for λ_m^2 and there exists N coefficients d_{mj} to be computed for each eigenvalue. Because the system is linear, one coefficient is to be selected arbitrarily, e.g. $d_{mm} = 1$. Following the computation of λ_m^2 and d_{mj}, Eq. (9) is to be written for each eigenvalue λ_m^2, that is,

$$\Psi_m = \sum_{j=1}^{N} d_{mj} f_j(y, z) \tag{18}$$

and then, the temperature solution becomes

$$T(y, z; x) = \sum_{m=1}^{N} B_m \Psi_m(y, z) \mathrm{e}^{-\lambda_m^2 x}. \tag{19}$$

In summary, the computation begins by finding the elements of matrices, **A** and **B**, and, then, Eq. (17) yields the eigenvalues λ_m^2. For each eigenvalue, the corresponding coefficients d_{mj} serve as the eigenvector. If the eigenvectors are placed within a row of a matrix designated as **D**, then the matrices **B** and **D** are numerically known and one can obtain the matrix $P = [(\mathbf{D}\cdot\mathbf{B})^{\mathrm{T}}]^{-1}$; that is, the matrix **D** is multiplied by matrix **B** and the resulting matrix is transposed and then inverted. By designating the elements of matrix **P** as p_{mi}, the coefficient B_m for inclusion in Eq. (19) is

$$B_m = \sum_{i=1}^{N} p_{mi} \int_A \rho c_p u(y, z) T(y, z; 0) f_i(y, z)\,\mathrm{d}A. \tag{20}$$

When $T(y,z;0)$ is prescribed at inlet, the temperature solution is obtainable [3] from the relation

$$T(y, z; x) = \frac{1}{\rho c_p} \int_A \sum_{m=1}^{\infty} \left[\sum_{i=1}^{N} p_{mi} \rho c_p u(y', z') f_i(y', z') \right] \times \left[\sum_{j=1}^{N} d_{mj} f_j(y, z) \right] \mathrm{e}^{-\lambda_m^2 x} T(y', z'; 0)\,\mathrm{d}A'. \tag{21}$$

The general formulation of the Green's function solution [3,5] is

$$T(y, z; x) = \frac{1}{\rho c_p} \left\{ \int_{\xi=0}^{x} \mathrm{d}\xi \int_\Gamma k_e \left(G\frac{\partial T}{\partial n} - T\frac{\partial G}{\partial n} \right)_{\Gamma'} \mathrm{d}\Gamma' + \int_{\xi=0}^{x} \mathrm{d}\xi \int_A GS(y', z'; \xi)\,\mathrm{d}A' + \int_A \rho c_p u(y', z') G(y, z, x \mid y', z', 0) T(y', z'; 0)\,\mathrm{d}A' \right\}. \tag{22}$$

By retaining only the third term on the right side of the Green's function solution, then Eq. (22) describes the same solution designated by Eq. (21) and; therefore, their comparison shows the Green's function,

$$G(y, z, x \mid y', z', \xi) = \sum_{m=1}^{N} \left[\sum_{i=1}^{N} p_{mi} f_i(y', z') \right] \Psi_m(y, z) \mathrm{e}^{-\lambda_m^2 (x-\xi)}. \tag{23}$$

In these derivations, the fully developed velocity $u(y,z)$, appearing is Eqs. (20)–(22) is treated as a known function. If the solution of Eq. (1) is not readily available, the computation of velocity $u(y,z)$ follows a similar procedure but with different numerical steps. For flow through a porous passage, the minimization of the functional I

$$I = \int_A \left[k_e \left(\frac{\partial u}{\partial y} \right)^2 + k_e \left(\frac{\partial u}{\partial z} \right)^2 + \left(\frac{\mu}{K} \right) u^2 + 2 \left(\frac{\partial p}{\partial x} \right) u \right] \mathrm{d}A, \tag{24a}$$

as described earlier, leads to the relation

$$\int_A \left[\mu_e \left(\frac{\partial^2 u}{\partial y^2} + \frac{\partial^2 u}{\partial z^2} \right) - \frac{\mu}{K} u - \frac{\partial p}{\partial x} \right] \eta_i\,\mathrm{d}A = 0. \tag{24b}$$

The method of solution, using Eq. (24b), is known as the method of weighted residuals or the Galerkin method. It begins by setting

$$u(y,z) = \sum_{j=1}^{N} \delta_j \eta_j(y,z). \tag{25}$$

For most cases, the basis function $\eta_j(y,z)$ for velocity, in Eq. (25), is the same as $f_j(y,z)$ for temperature if its boundary condition is of the first kind. For example, they become different if velocity is zero at the wall while the temperature gradient is zero there. Next, the substitution of $u(y,z)$ from Eq. (25) in Eq. (24b), leads to a set of simultaneous equations and, in the matrix form, they are

$$\mathbf{E} \cdot \Delta = \Omega, \tag{26a}$$

where the matrix $\mathbf{E}$ has elements

$$e_{ij} = \int_A [\mu_e \eta_i(\mathbf{y},z)\nabla^2 \eta_j(\mathbf{y},z) - \mu\eta_j/K]\,\mathrm{d}A \tag{26b}$$

the vector Ω has elements

$$\omega_i = \left(\frac{\partial p}{\partial x}\right) \int_A \eta_i(y,z)\,\mathrm{d}A \tag{26c}$$

while the unknowns, $(\delta_1, \delta_2, \ldots, \delta_N)$, are the elements of vector $\Delta = \mathbf{E}^{-1} \cdot \Omega$.

Following the determination of the Green's function, Eq. (23), the temperature solution, Eq. (22), is known. The application of energy balance on a fluid element leads toward the evaluation of the heat transfer coefficient. It is best to accomplish this task in the dimensionless space. Therefore, it is necessary to define a characteristic length L_c and a dimensionless temperature $\theta = (T - T_2)/(T_1 - T_2)$ where T_1 and $T_2 \neq T_1$ are two constant temperatures. In the subsequent formulations, T_1 stands for the inlet temperature and T_2 stands for the wall temperature. One can define other dimensionless quantities $\bar{y} = y/L_c$, $\bar{z} = z/L_c$, $M = \mu_e/\mu$, $Da = K/L_c^2$, $Re_D = \rho U D_h/\mu_e$, $Pr = \mu_e c_p/k_e$, $Ec = U^2/[c_p(T_1 - T_2)]$ and $\bar{x} = (x/D_h)/(Re_D Pr)$, the local heat transfer coefficient is

$$Nu_D = \frac{hD_h}{k} = -\left(\frac{1}{4}\right)\left[\frac{\mathrm{d}\theta_b(\bar{x})/\mathrm{d}\bar{x}}{\theta_b(\bar{x})}\right] + \left(\frac{D_h}{2L_c}\right)^2 \left[\frac{EcPr}{\theta_b(\bar{x})}\right] S^*, \tag{27a}$$

that includes the effect of frictional heating since

$$S^* = \frac{1}{\bar{A}} \int_{\bar{A}} \left[\frac{(u/U)^2}{MDa} + \left(\frac{\partial(u/U)}{\partial \bar{y}}\right)^2 + \left(\frac{\partial(u/U)}{\partial \bar{z}}\right)^2\right] \mathrm{d}\bar{y}\,\mathrm{d}\bar{z} \tag{27b}$$

wherein $\bar{A}$ is the dimensionless area. This method of analysis is used also to solve transient heat conduction problems in [3] and it is an extension of the method of weighted residuals. As shown in [4], in comparison with the exact series solution, it provides acceptable accuracies at larger values $\bar{x}$ and better accuracies at smaller $\bar{x}$, when using the same number of eigenvalues. Another interesting feature is embedded in the details of the computational procedure. Except for the basis function and integration over the specific domain, all other steps are the same for all cases studied.

The method of selecting the basis functions, for the boundary conditions of the first kind, is widely available in the literature; see the Galerkin method in [2]. A procedure for selecting basis functions for the boundary conditions of the second kind is in [3, p. 342] and for the boundary conditions of the third kind is in [3, p. 345]. The primary illustration is devoted to selection of the basis functions for the boundary conditions of the first kind at the wall for a few selected passages. They are

1. For flow between two parallel plates with walls located at $y = \pm H$,
   $$f_j = [1 - (y/H)^2](y/H)^{2(j-1)} \quad \text{with } j = 1, 2, \ldots, N.$$
2. For a circular pipe with radius r_0, the basis functions are similar,
   $$f_j = [1 - (r/r_0)^2](r/r_0)^{2(j-1)} \quad \text{with } j = 1, 2, \ldots, N.$$
3. For a rectangular passage with walls located at $y = \pm a$ and $z = \pm b$,
   $$f_j = (a^2 - y^2)(b^2 - z^2)y^{2(m_j-1)}z^{2(n_j-1)},$$
   using all combination of m_j and n_j.
4. For an elliptical passage with the wall being at $(y/a)^2 + (z/b)^2 = 1$,
   $$[1 - (y/a)^2 - (z/b)^2]y^{2(m_j-1)}z^{2(n_j-1)},$$
   using all combinations of m_j and n_j.
5. For an isosceles triangular passage with walls located at $z = \pm by/a$ and $z = b$,
   $$[z^2 - (by/a)^2](z - b)y^{2(m_j-1)}z^{(n_j-1)},$$
   using all combinations of m_j and n_j.

In general, any independent and complete set of functions can serve as the basis functions. For example, $\cos[(j - 1/2)\pi y/H]$ and $\cos[(j - 1/2)\pi r/r_0]$ can replace those listed above for parallel-plate channels and circular passages, respectively.

4. Numerical illustrations

Having an ordered set of basis functions, Eqs. (25) and (26) yield the velocity distribution. The next step is the computation of matrices $\mathbf{A}$ and $\mathbf{B}$ using Eqs. (16a) and (16b). These and other major operations are summarized and shown for one and two-dimensional passages.

4.1. One-dimensional passages

These types of passages are useful mainly to evaluate the accuracy of this procedure before applying it to more difficult problems. The examples for this case are limited to parallel-plate channels and circular pipes for which an exact solution is available. This enables one to compare the computed results to evaluate the accuracy as well as the utility of this EWR technique.

4.1.1. Numerical Example 1

In this example, the study of heat transfer in circular pipes, when $M\,Da = \infty$, is selected for two reasons: (a) to demonstrate the procedure and (b) to investigate the accuracy of this methodology by comparing the results with those from exact analysis. A brief Mathematica program [13] written to perform the basic steps for a circular pipe when $e = 1$ and for a parallel-plate channel $e = 0$.

```
(*amat = A,    bmat = B.    dmat = D,    pmat = P,
cap = capacitance/ke,   u = velocity,   eigv = eigenvalues
vector *)
   Off[General::spell1];
   e = 1; n = 10; cap = 1; u = (3/2 + e/2)*(1−r^2); uav = 1;
   fi = (1−r^2)*r^(2*i − 2); fj = (1−r^2)*r^(2*j − 2);
   oper = Simplify[fi*(r^e*D[D[fj,r],r]+e*D[fj,r])];
   amat = Table[Integrate[oper, {r,0,1}], {i,1,n}, {j,1,n}];
   bmat = Table[Integrate[cap*u*r^e*fi*fj/uav, {r,0,1}],
          {i,1,n}, {j,1,n}];
   amat = N[amat,300]; bmat = N[bmat,300];
   eigv = N[Eigenvalues[-Inverse[bmat].amat]];
   dmat = Eigenvectors[-Inverse[bmat].amat];
   pmat = Inverse[Transpose[dmat.bmat]];
```

This program is in dimensionless space by setting $r_0 = 1$ and u stands for u/U. It is remarkable that these few statements produce all needed information to get the Green's function from Eq. (23). Currently, this program is for an unobstructed circular pipe since $e = 1$ and it becomes the solution for a parallel-plate channel by setting $e = 0$. The remaining steps are the evaluation and utilization of computed temperature and they begin by using Eq. (22); they are

```
Do[psi[ne] = Sum[dmat[[ne,j]]*fj, {j,1,n}], {ne,1,n}];
     temp = Sum[psi[ne]*Exp[-eigv[[ne]]*x]*Sum[pmat[
              [ne,i]]*Integrate[r^e*cap*fi*u/uav,
              {r,0,1}], {i,1,n}], {ne,1,n}];
   tbulk = (1 + e)*Integrate[r^e*temp*u/uav, {r,0,1}];
```

Table 1 shows a set of 40 eigenvalues computed by the EWR method for a circular passage. They are compared to the first 40 eigenvalues obtained by the exact analysis [14]. The selection of an unobstructed circular pipe eliminates the expected numerical error because the values of a_{ij} and b_{ij} are determined exactly. The first 16 eigenvalues in Column 2 have the same 8 significant figures as those in Column 3. Indeed, the first eigenvalue λ_1^2 for EWR is 3.6567934577632926 when using 40 terms and, when using 70 terms, it becomes 3.656793457763292361. The two computed values of λ_1^2 compare favorably with 3.656793457763292362 obtained through exact analysis. Beyond 16, the EWR eigenvalues begin to increase faster than those by exact analysis; for the 40th eigenvalue the

Table 1
A comparison of the first 40 eigenvalues for circular porous passages

m	EWR method	Exact	m	EWR method	Exact
1	3.6567935	3.6567935	21	3494.4736	3416.9254
2	22.304731	22.304731	22	3985.4293	3755.5915
3	56.960515	56.960515	23	4626.1452	4110.2576
4	107.62027	107.62027	24	5468.0498	4480.9238
5	174.28206	174.28206	25	6585.1737	4867.5900
6	256.94503	256.94503	26	8088.7458	5270.2562
7	355.60877	355.60877	27	10149.731	5688.9224
8	470.27303	470.27303	28	13037.954	6123.5887
9	600.93767	600.93767	29	17193.062	6574.2550
10	747.60260	747.60260	30	23358.930	7040.9213
11	910.26775	910.26775	31	32851.305	7523.5876
12	1088.9331	1088.9331	32	48123.367	8022.2539
13	1283.5986	1283.5986	33	74048.592	8536.9202
14	1494.2642	1494.2642	34	121092.65	9067.5866
15	1720.9298	1720.9298	35	214044.37	9614.2530
16	1963.5956	1963.5956	36	419598.56	10176.919
17	2222.2636	2222.2615	37	951155.63	10755.586
18	2497.0160	2496.9274	38	2686677.0	11350.252
19	2789.3513	2787.5933	39	11045617.1	11960.919
20	3110.6168	3094.2594	40	97924166.7	12587.585

Table 2
A comparison of computed local and average Nusselt numbers by EWR method and exact analysis

$(x/r_0)/Pe$	Local Nu		Average Nu		Exact solution[a]	
	EWR[b]	Exact[b]	EWR[b]	Exact[b]	Local Nu	Average Nu
0.000001	169.856	43.6241	255.240	1426.46	155.009	236.929
0.00001	78.2216	42.3854	117.867	217.150	78.2213	117.867
0.0001	35.8059	33.4468	54.1737	55.4381	35.8059	54.1736
0.001	16.2640	16.2640	24.7226	24.7226	16.2640	24.7225
0.01	7.47038	7.47038	11.2690	11.2690	7.47038	11.2690
0.1	4.00463	4.00463	5.46820	5.46820	4.00463	5.46820
1	3.65679	3.65679	3.85640	3.85640	3.65679	3.85640
10	3.65679	3.65679	3.67675	3.67675	3.65679	3.67675

[a] Exact solution using 500 eigenvalues, $\lambda_{500}^2 = 1.9973342 \times 10^6$.
[b] Using 40 eigenvalues.

difference is very significant. The larger eigenvalues would permit acquisition of more accurate data as $\bar{x} = (x/r_0)/Pe$ becomes very small.

To demonstrate the accuracy of these two methods, Table 2 presents the values of the local and average Nusselt numbers for a relatively large range of $\vec{x}$. When $\bar{x} \geqslant 10^{-3}$, the recorded data in columns 2 and 3, for the local Nusselt number, and in columns 4 and 5, for the average Nusselt number, are the same. However, these Nusselt number data begin to depart from each other as $\vec{x}$ decreases. When $\bar{x} \leqslant 10^{-5}$, the difference becomes very large. In the exact analysis, the eigenvalues rapidly approach $\lambda_m \cong [4(m-1)+8/3]/\sqrt{2}$ as m in Eq. (23) becomes large, indicating a constant spacing $\cong 4/\sqrt{2}$; whereas, in the EWR method, the spacing between eigenvalues increases as m increases. Setting $e = 0$ in this Mathematica program for flow between parallel plates, the larger computed eigenvalues also depart from $\lambda_m \cong [4(m-1)+5/3]/\sqrt{3/2}$ that describes a limit for the eigenvalues from exact analysis.

To verify the accuracy of the tabulated data, the local and average Nusselt numbers are computed, by exact analysis, using 500 eigenvalues and they are tabulated in columns 6 and 7. Since the largest eigenvalue for $m = 500$ is $\lambda_{500}^2 = 1.997 \times 10^6$, good accuracy is expected at $\bar{x} = 10^{-4}$ and, at this value of $\bar{x}$, the data agree favorably with EWR data in Columns 2 and 4. Also, it is appropriate to demonstrate the accuracy of EWR data by increasing the number of eigenvalues. Repeating the EWR procedure when $N = 60$, all computed values agree with those in Table 2 except for $\bar{x} = 10^{-6}$, at which, the computed local and average Nusselt numbers are 169.761 and 255.212, respectively. These also agree reasonably well with 169.856 and 255.240 entries in Table 2. Moreover, increasing the number of terms to $N = 70$, with $\lambda_{70}^2 = 2.5615 \times 10^9$, produced the above results obtained for $N = 60$, with $\lambda_{60}^2 = 1.0373 \times 10^9$. This presents significant information as this minimization concept increases the size of the larger eigenvalues in order to enhance the accuracy of the computed data within the computational domain.

When using Eq. (22) to compute the temperature distribution, the first two terms on the right side require integration over the axial coordinate from 0 to x. Often, the upper limit, following integration, does not converge to its fully-developed value. Remedial steps to improve the convergence for the exact analysis are in [5]. However, the EWR method does converge to its fully developed value as x becomes large. As an illustration, for pipe plow in Example 1, the dimensionless wall heat flux due to frictional heating alone has a value of 4 when $x = \infty$. Using 60 terms, the exact solution of dimensionless wall heat flux is 3.75; however, the EWR method produced the correct value of 4 with no need for a remedial step.

4.2. Two-dimensional passages

The application of Eqs. (22) and (23) leads to a temperature solution in two-dimensional passages. When L_c is a characteristic length and the hydraulic diameter is $D_h = 4A/C$, using the dimensionless quantities $\bar{y} = y/L_c$, $\bar{z} = z/L_c$, and $\bar{x} = (x/D_h)/(Re_D Pr)$, Eq. (5) takes the form

$$\left(\frac{D_h}{L_c}\right)^2 \left(\frac{\partial^2 T}{\partial \bar{y}^2} + \frac{\partial^2 T}{\partial \bar{z}^2}\right) + \bar{S}(\bar{y}, \bar{z}; \bar{x}) = \frac{\partial T}{\partial \bar{x}}, \tag{28a}$$

where $\bar{S}(\vec{y}, \bar{z}; \bar{x}) = D_h^2 S(y, z; x)/k_e$ is the dimensionless volumetric heat source,

$$\bar{S}(\vec{y}, \bar{z}; \bar{x}) = \frac{\mu_e (U D_h)^2}{k_e L_c^2} \left[\frac{(u/U)^2}{MDa} + \left(\frac{\partial (u/U)}{\partial \bar{y}}\right)^2 + \left(\frac{\partial (u/U)}{\partial \bar{z}}\right)^2\right]. \tag{28b}$$

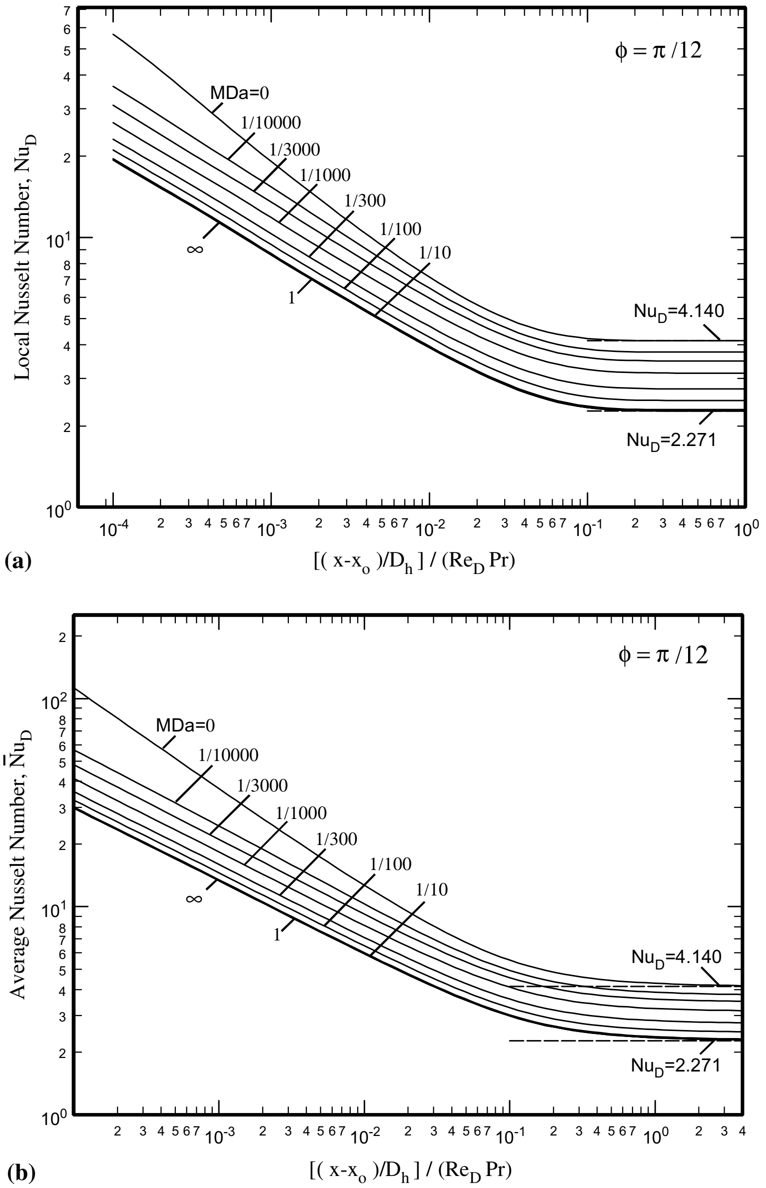

Fig. 2. Computed Nusselt numbers for flow through isosceles triangular passages with $2\phi = 30°$: (a) local values and (b) average values.

Following the computation of the velocity and temperature distributions, Eq. (27a) provides the value of the Nusselt number. Once the bulk temperature is known, the energy equation as applied to a volume element leads to the relation

$$q_w C\,dx + dx\int_A \left\{\mu u^2/K + \mu_e[(\partial u/\partial y)^2 + (\partial u/\partial z)^2]\right\} dA = \rho A U c_p\, dT_b, \tag{29a}$$

where q_w is the circumferentially averaged wall heat flux. In dimensionless form, Eq. (29a) becomes

$$\begin{aligned}\frac{q_w D_h}{k_e(T_1 - T_2)} &= -\left(\frac{\mu_e c_p}{k_e}\right)\frac{U^2(D_h/L_c)^2}{4c_p(T_1 - T_2)}S^* \\ &\quad + \frac{1}{4}Re_D Pr\frac{d[(T_b - T_2)/(T_1 - T_2)]}{d(x/D_h)} \\ &= -\left(\frac{D_h}{2L_c}\right)^2 Pr Ec S^* + \frac{1}{4}\frac{d\theta_b}{d\bar{x}},\end{aligned} \tag{29b}$$

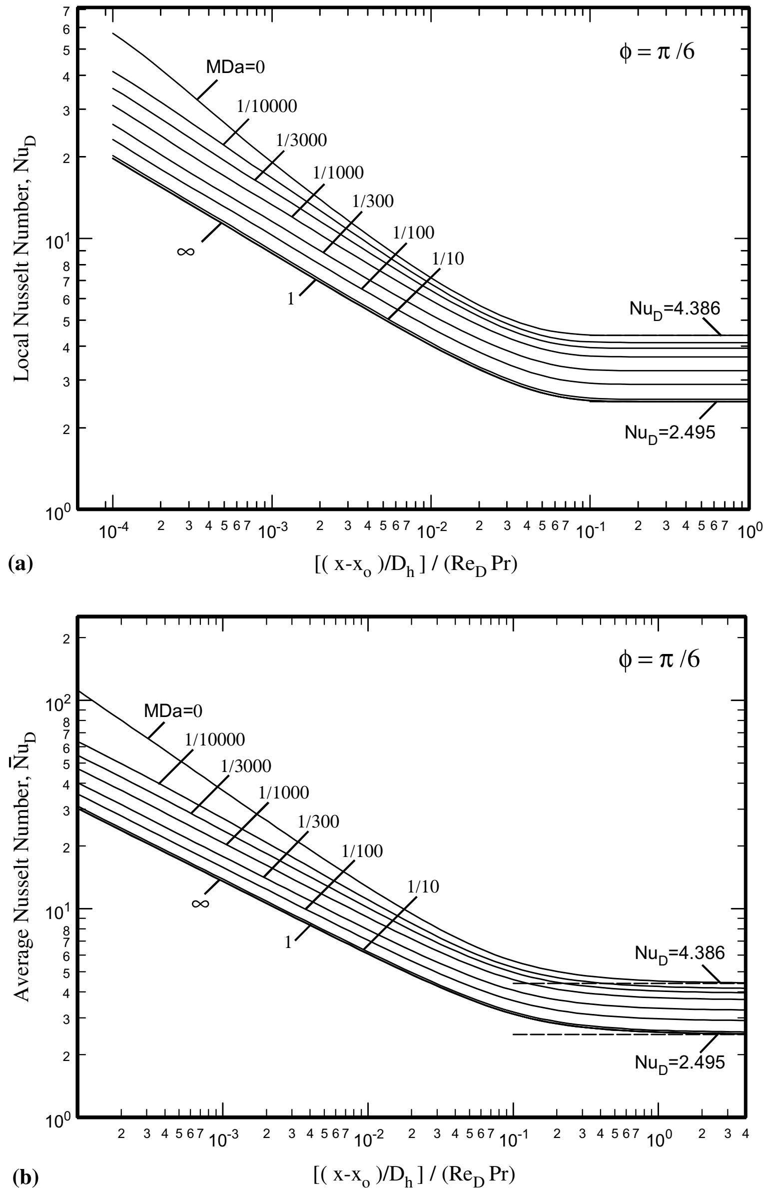

Fig. 3. Computed Nusselt numbers for flow through isosceles triangular passages with $2\phi = 60°$: (a) local values and (b) average values.

where S^* was defined in Eq. (27b) and $\theta_b = (T_b - T_2)/(T_1 - T_2)$. Since S^* in Eq. (27b) is a constant and $\theta_b(0) = 0$, the integration of this relation is readily available from the relation

$$\frac{\bar{q}_w D_h}{k_e(T_2 - T_1)} = \frac{1}{\bar{x}} \int_{\bar{x}=0}^{\bar{x}} \frac{q_w D_h}{k_e(T_2 - T_1)} \mathrm{d}\bar{x} = -\left(\frac{D_h}{2L_c}\right)^2 PrEcS^* + \frac{1}{4}\theta_b(\bar{x}). \tag{30}$$

4.2.1. Numerical Example 2

To demonstrate the utility of this solution method, it is appropriate to study heat transfer to a fluid passing through a passage and there is no classical exact solution available. For this reason, isosceles triangular passages filled with saturated porous materials are being considered. The cross-section of this passage is shown in Fig. 1(b). Of course, when $2\phi = 60°$ then $W = H/\sqrt{3}$, and the fully developed velocity profile has an exact solution for an unobstructed channel, it is

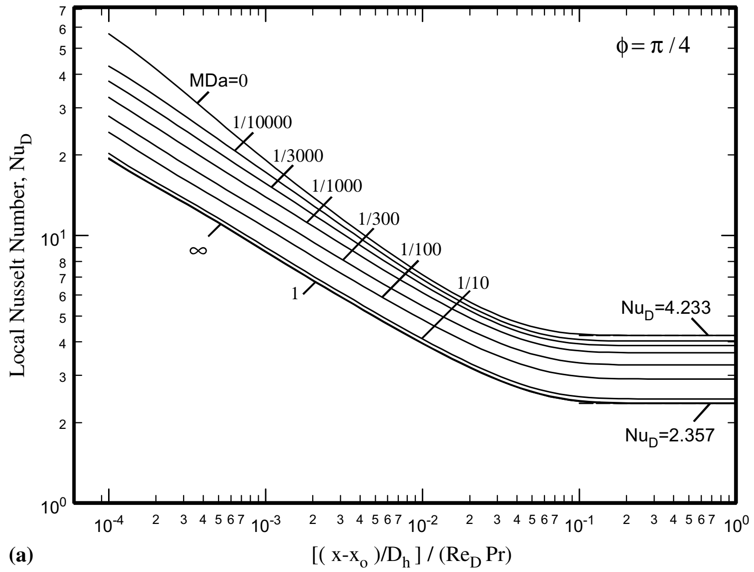

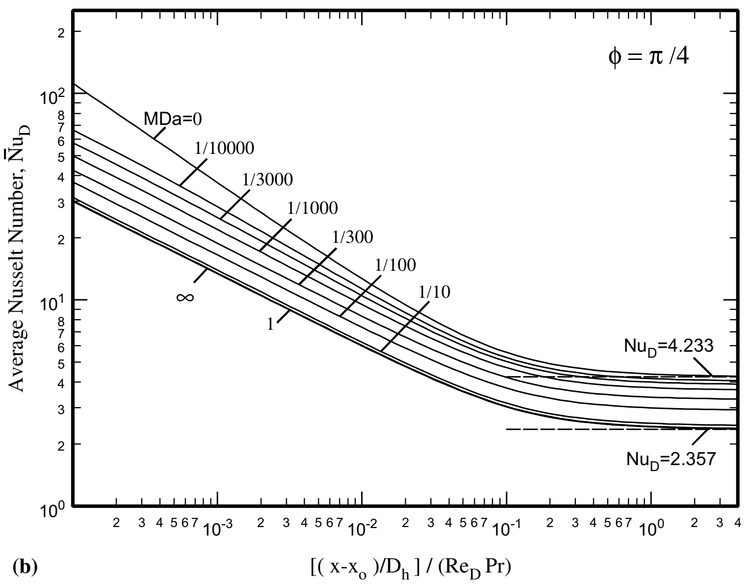

Fig. 4. Computed Nusselt numbers for flow through isosceles triangular passages with $2\phi = 90°$: (a) local values and (b) average values.

$$u = \left(\frac{-H^2}{4\mu}\frac{\partial p}{\partial x}\right)\left(1 - \frac{y}{W}\right)\left[\left(\frac{y}{W}\right)^2 - 3\left(\frac{x}{W}\right)^2\right]. \tag{31}$$

However, in general and specifically for flow through a porous passage, Eqs. (24)–(26) would provide the velocity distribution. The procedure is similar to that described for flow through the circular passages. There are a few modifications: first, to provide a fully developed velocity profile for the given configuration. Next, one must select an appropriate set of basis functions and perform all area integrations over the specified triangular domain. All other steps remain as described in Example 1.

This example considers the effects of wall temperature change and volumetric heat source when using the boundary condition of first kind. It considers two effects: one due to a temperature change at the wall and the second due to the frictional heating. First, consideration is given to a case when the fluid has a constant temperature T_1 at $x = 0$ and the wall temperature remains at $T = T_1$ until at $x = x_0$ where there is a surface temperature change $T = T_2$. Next, the effect of frictional heating is to begin at $x = 0$ and remains throughout the passage. Using a dimensionless temperature $\theta = (T - T_1)/(T_2 - T_1)$, in Eq. (22), the effect of temperature change at the wall is

$$\frac{T - T_2}{T_1 - T_2} = \int_{y=0}^{W} \int_{Hy/W}^{H} u(y', z') \times G(y, z, x - x_0 \mid y', z', 0)\, \mathrm{d}y'\, \mathrm{d}z' \tag{32a}$$

that yields

$$\frac{T - T_1}{T_2 - T_1} = 1 - \frac{T - T_2}{T_1 - T_2} = 1 - \int_{y'=0}^{W} \int_{z'=Hy/W}^{H} u(y', z') \times G(y, z, x - x_0 \mid y', z', 0)\, \mathrm{d}y'\, \mathrm{d}z'. \tag{32b}$$

The contribution of the volumetric heat source, to be added to this equation, is

$$\int_{\xi=0}^{x} \int_{y'=0}^{W} \int_{z'=Hy/W}^{H} \left\{ \frac{\mu[u(y', z')]^2}{K} + \mu_e \left[\left(\frac{\partial u(y', z')}{\partial y'} \right)^2 + \left(\frac{\partial u(y', z')}{\partial z'} \right)^2 \right] \right\} \times G(y, z, x \mid y', z', \xi)\, \mathrm{d}z'\, \mathrm{d}y'\, \mathrm{d}\xi \tag{33}$$

and the functional form of $G(y, z, x|y', z', \xi)$ is in Eq. (23).

The program to perform these computations was also written in Mathematica symbolic computer language [13]. First, a velocity profile was computed in accordance to Eqs. (25) and (26). Basically, the same program presented in Example 1 was used to compute the temperature distribution except for obvious modifications. They are: (a) using an appropriate set of basis functions for isosceles triangular passages and (b) performing the integrations over the cross-section of an isosceles triangular passage.

To show the effect of a temperature change at the wall, the local and average Nusselt numbers are computed. Indeed, a local heat flux, in this example, is a circumferentially averaged quantity used to determine the local Nusselt number. Basic heat transfer information are prepared for three isosceles triangular passages, $2\phi = 30°$, $60°$, and $90°$. When $2\phi = 30°$ and with no frictional heating effects, Fig. 2(a) shows the value of the local Nusselt number as a function of the axial coordinate for different values of $MDa; = (\mu_e/\mu)(K/H^2)$. It is prepared following the computation of bulk temperature. Fig. 2(b) shows the variation of average Nusselt number for the same range of variables as in Fig. 2(a). The computation of local and average Nusselt numbers are repeated for angle $2\phi = 60°$ for which the fully developed velocity profile is known and the results are in Fig. 3(a) and (b). Similarly, the data in Fig. 4(a) and (b) show the local and average Nusselt numbers for a larger angle $2\phi = 90°$.

The second part of this example is devoted to the computation of bulk temperature solely due to the effect of frictional heating. In the absence of a wall temperature change and for convenience of the presentation, Eq. (29b) takes an alternative form,

$$\frac{q_w D_h}{\mu_e U^2} = -\left(\frac{D_h}{2L_c} \right)^2 S^* + \frac{1}{4} \frac{d[(T_b - T_1)/(\mu_e U^2)]}{\mathrm{d}\bar{x}}. \tag{34}$$

Fig. 5(a) depicts the values of the dimensionless local heat flux $q_w D_h/(\mu_e U^2)$ and average heat flux $\bar{q}_w D_h/(\mu_e U^2)$ when $2\phi = 30°$. The data show the influence of the same set of MDa values as plotted in Fig. 2(a), but not when $MDa = 0$. The computations are repeated for $2\phi = 60°$ and $90°$; Fig. 5(b) is for $2\phi = 60°$ and Fig. 5(c) is for $2\phi = 90°$.

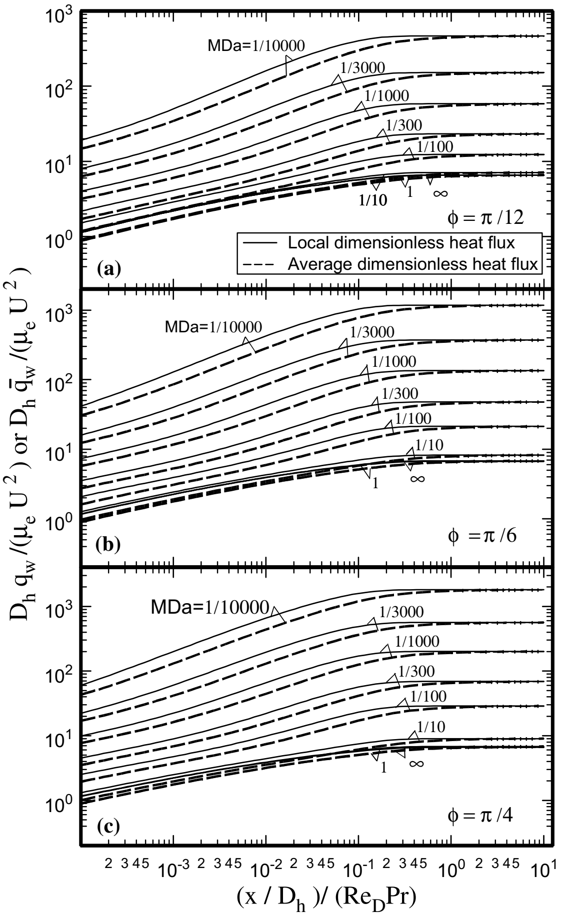

Fig. 5. Local and average wall heat flux due to frictional heating for flow through isosceles triangular passages: (a) with $2\phi = 30°$, (b) with $2\phi = 60°$, and (c) with $2\phi = 90°$.

5. Discussion and comments

A summary of the computed values is prepared in order to illustrate the numerical characteristics of the dimensionless quantities. The data in Figs. 2–5 are acquired using the basis function

$$[z^2 - (Hy/W)^2](z - H)y^{2(m_j-1)}z^{(n_j-1)}$$

with $m_j = 1,2,\ldots,8$ and $n_j = 1,2,\ldots,15$. Therefore, 120 basis functions make the working matrices of the size 120×120. Selected computations were repeated using 91 basis functions in order to verify the accuracy of the results. Small deviations were observed at small values of $\bar{x}$. For $2\phi = 30°$, Table 3 shows the computed numerical values using a relatively small range of the axial coordinate and MDa values. When $MDa = \infty$, the data in Table 3 agree well with those reported in [15].

In this example, the data related to local and average Nusselt numbers are valid when heating (or cooling) begins at $x = x_0$ and $0 \leqslant x_0 \leqslant \infty$. Accordingly, the coordinate $\bar{x}$ is defined so that the heating begins at the dimensionless axial coordinate $\bar{x} = [(x - x_0)/D_h]/$

Table 3
Selected heat transfer variables for isosceles triangular passages when $2\phi = 30°$

MDa	$\bar{x}$	Nu_D	$\overline{Nu}_D$	$\theta_{b,I}$	q_w^*	$\bar{q}_w^*$	$\theta_{b,S}$
1/10000	0.0001	36.363	56.616	0.97761	19.108	14.700	0.18079
	0.001	15.392	24.425	0.90692	49.928	34.580	1.7284
	0.01	6.4922	10.314	0.66195	160.22	106.60	14.403
	0.1	3.8504	4.9469	0.13824	402.47	298.67	67.202
	1	3.7567	3.8798	1.82×10^{-7}	466.67	445.64	84.131
	10	3.7567	3.7690	3.35×10^{-66}	466.67	464.57	84.131
1/1000	0.0001	26.624	41.371	0.98359	4.0146	3.1625	0.022084
	0.001	11.844	18.348	0.92924	7.8467	6.0371	0.20934
	0.01	5.3351	8.1326	0.72231	18.749	13.382	1.7996
	0.1	3.2380	4.1049	0.19360	47.590	34.737	9.4540
	1	3.1413	3.2423	2.33×10^{-6}	58.371	55.159	12.851
	10	3.1413	3.1514	1.80×10^{-55}	58.372	58.050	12.851
1/100	0.0001	21.126	32.528	0.98707	1.5193	1.1806	0.0044935
	0.001	9.4013	14.553	0.94345	2.8878	2.2648	0.040598
	0.01	4.2664	6.4870	0.77145	5.2633	4.1674	0.32988
	0.1	2.5654	3.2679	0.27059	9.9659	7.8213	1.8372
	1	2.4855	2.5675	3.47×10^{-5}	12.414	11.711	2.8126
	10	2.4855	2.4937	4.79×10^{-44}	12.414	12.344	2.8127
1/10	0.0001	19.593	30.135	0.98802	1.1750	0.90704	0.0024949
	0.001	8.7094	13.485	0.94749	2.2674	1.7710	0.021493
	0.01	3.9497	6.0097	0.78632	3.9496	3.2019	0.15770
	0.1	2.3681	3.0204	0.29875	6.1154	5.1686	0.79025
	1	2.2973	2.3728	7.55×10^{-5}	7.1440	6.8363	1.2318
	10	2.2973	2.3049	9.12×10^{-41}	7.1443	7.1135	1.2320
1	0.0001	19.389	29.824	0.98814	1.1384	0.87800	0.0022865
	0.001	8.6189	13.346	0.94802	2.2026	1.7190	0.019501
	0.01	3.9091	5.9478	0.78827	3.8215	3.1056	0.13954
	0.1	2.3435	2.9891	0.30252	5.7333	4.9093	0.67396
	1	2.2741	2.3487	8.32×10^{-5}	6.5939	6.3325	1.0465
	10	2.2741	2.2815	2.32×10^{-40}	6.5942	6.5680	1.0466
10	0.0001	19.368	29.792	0.98815	1.1348	0.87508	0.0022655
	0.001	8.6095	13.331	0.94807	2.1961	1.7138	0.019300
	0.01	3.9049	5.9414	0.78847	3.8087	3.0960	0.13772
	0.1	2.3410	2.9858	0.30291	5.6951	4.8834	0.66217
	1	2.2717	2.3462	8.40×10^{-5}	6.5386	6.2819	1.0276
	10	2.2717	2.2791	2.56×10^{-40}	6.5388	6.5132	1.0277
∞	0.0001	19.365	29.788	0.98816	1.1344	0.87475	0.0022632
	0.001	8.6085	13.330	0.94808	2.1954	1.7132	0.019278
	0.01	3.9044	5.9407	0.78850	3.8073	3.0949	0.13751
	0.1	2.3407	2.9855	0.30295	5.6909	4.8806	0.66085
	1	2.2714	2.3459	8.41×10^{-5}	6.5325	6.2763	1.0255
	10	2.2714	2.2789	2.58×10^{-40}	6.5327	6.5071	1.0256

($Re_D Pr$). However, the frictional heating generally begins at $x = 0$ and in dimensionless form, the coordinate $\bar{x} + \bar{x}_0 = (x/D_h)/(Re_D Pr)$ stands for the physical coordinate x. In these tables, the dimensionless heat flux values are designated as $q_w^* = q_w D_h/(\mu_e U^2)$ and $\bar{q}_w^* = \bar{q}_w D_h/(\mu_e U^2)$. The data include the dimensionless bulk temperature $\theta_{b,w} = (T_b - T_1)/(T_2 - T_1) = 1 - \theta_{b,i}$ due the wall temperature change alone while $\theta_{b,s} = [(T_b - T_1)/(T_2 - T_1)]/(PrEc)$ or $\theta_{b,s} = k_e(T_b - T_1)/(\mu_e U^2)$ due to the sole effect of the frictional heating. Of course the actual bulk temperature is the sum of these two bulk temperatures at $x \geqslant x_0$ for all values of x_0. The data in Table 3 are prepared when $2\phi = 30°$. When $2\phi = 60°$, the corresponding data are in Table 4, and when $2\phi = 90°$, they are in Table 5. The data in these tables are accurate to all 5 reported digits when $\bar{x}$ is relatively large. However, when $\bar{x}$ is very small, the accuracy reduces to 3–4 significant digits. Although the data in

Table 4
Selected heat transfer variables for isosceles triangular passages when $2\phi = 60°$

$M\,Da$	$\bar{x}$	Nu_D	$\overline{Nu}_D$	$\theta_{b,I}$	q_w^*	$\bar{q}_w^*$	$\theta_{b,S}$
1/10000	0.0001	41.319	63.495	0.97492	41.697	30.613	0.46005
	0.001	16.690	27.179	0.89698	128.96	85.669	4.3802
	0.01	6.7860	11.064	0.64241	424.55	282.33	35.936
	0.1	4.1509	5.2373	0.12308	1035.7	775.28	162.18
	1	4.1298	4.2410	4.29×10^{-8}	1180.7	1131.4	197.26
	10	4.1298	4.1409	1.16×10^{-72}	1180.7	1175.8	197.26
1/1000	0.0001	30.992	47.080	0.98134	7.3260	5.7175	0.051764
	0.001	13.300	20.740	0.92039	15.646	11.627	0.49400
	0.01	5.9064	9.0943	0.69505	43.775	29.906	4.2089
	0.1	3.6814	4.5796	0.16012	113.90	83.239	20.756
	1	3.6553	3.7483	3.08×10^{-7}	135.13	128.49	26.552
	10	3.6553	3.6646	2.19×10^{-64}	135.13	134.46	26.553
1/100	0.0001	23.182	35.594	0.98586	2.0829	1.6075	0.0079049
	0.001	10.271	15.829	0.93865	3.9276	3.0832	0.073146
	0.01	4.6695	7.0771	0.75346	7.7548	5.9321	0.61750
	0.1	2.9217	3.6281	0.23428	17.112	12.840	3.4118
	1	2.8960	2.9698	6.93×10^{-6}	21.370	20.150	4.8794
	10	2.8960	2.9034	3.65×10^{-51}	21.370	21.248	4.8795
1/10	0.0001	20.214	31.095	0.98764	1.2648	0.96744	0.0029075
	0.001	9.0172	13.888	0.94596	2.4225	1.8972	0.025356
	0.01	4.1190	6.2296	0.77944	4.2811	3.4488	0.19150
	0.1	2.5747	3.1983	0.27823	6.9881	5.7907	0.97821
	1	2.5514	2.6167	2.85×10^{-5}	8.2361	7.8698	1.4656
	10	2.5514	2.5580	3.66×10^{-45}	8.2362	8.1996	1.4657
1	0.0001	19.7552	30.373	0.98792	1.1719	0.89485	0.0023721
	0.001	8.8196	13.578	0.94714	2.2584	1.7655	0.020239
	0.01	4.0345	6.0968	0.78359	3.9468	3.1999	0.14501
	0.1	2.5240	3.1339	0.28548	5.9779	5.1051	0.68804
	1	2.5012	2.5650	3.501×10^{-5}	6.8251	6.5690	1.0250
	10	2.5012	2.5076	2.75×10^{-44}	6.8252	6.7996	1.0251
10	0.0001	19.706	30.295	0.98796	1.1625	0.88749	0.0023180
	0.001	8.7985	13.545	0.94726	2.2418	1.7522	0.019721
	0.01	4.0255	6.0827	0.78403	3.9137	3.1751	0.14030
	0.1	2.5187	3.1271	0.28626	5.8771	5.0370	0.65820
	1	2.4959	2.5596	3.58×10^{-5}	6.6824	6.4378	0.97911
	10	2.4959	2.5023	3.40×10^{-44}	6.6825	6.6581	0.97915
∞	0.0001	19.701	30.286	0.98796	1.1615	0.88667	0.0023120
	0.001	8.7962	13.541	0.94728	2.2400	1.7507	0.019664
	0.01	4.0245	6.0811	0.78408	3.9101	3.1724	0.13977
	0.1	2.5181	3.1264	0.28635	5.8659	5.0295	0.65487
	1	2.4953	2.5590	3.59×10^{-5}	6.6666	6.4232	0.97399
	10	2.4953	2.5017	3.48×10^{-44}	6.6667	6.6423	0.97403

Tables 3–5 are for a special case when the wall temperature changes at $\bar{x}_0 = 0$, they can be also used when $\bar{x}_0 > 0$.

Another item observed is the behavior of the frictional wall heat flux when MDa becomes too small. Table 6 is prepared to show the limiting values of $q_w D_h/(\mu_e U^2)$, $\bar{q}_w D_h/(\mu_e U^2)$, and $\theta_{b,s}$ as $MDa \to 0$. They are obtained assuming the velocity in the porous passage is to approach a constant value. The data, obtained in this manner, agrees satisfactorily with those in Fig. 5(a)–(c) when $MDa = 10^{-4}$ and begins to gradually depart as MDa increases.

As expected, there is a significant heat flux variation along each surface of these triangular passages. To show the variations, the local wall heat flux is computed, when $2\phi = 30°$, for a different set of MDa values. The heat flux input along a sidewall, shown in Fig. 1(b), is computed using the relation,

Table 5
Selected heat transfer variables for isosceles triangular passages when $2\phi = 90°$

MDa	$\bar{x}$	Nu_D	$\overline{Nu}_D$	$\theta_{b,I}$	q_w^*	$\bar{q}_w^*$	$\theta_{b,S}$
1/10000	0.0001	42.944	66.444	0.97377	60.072	42.852	0.70375
	0.001	17.205	28.252	0.89314	199.72	130.57	6.6866
	0.01	6.8508	11.309	0.63612	657.91	438.32	54.556
	0.1	4.0841	5.2489	0.12251	1581.7	1189.1	245.25
	1	4.0311	4.1545	6.07×10^{-8}	1802.2	1727.3	299.73
	10	4.0311	4.0435	5.72×10^{-71}	1802.2	1794.7	299.73
1/1000	0.0001	32.777	49.802	0.98028	9.8355	7.6743	0.077186
	0.001	13.939	21.902	0.91612	22.275	16.198	0.73777
	0.01	6.1136	9.5007	0.68384	65.982	44.505	6.2454
	0.1	3.7057	4.6929	0.15303	170.31	125.07	30.227
	1	3.6454	3.7521	3.03×10^{-7}	200.64	191.02	38.504
	10	3.6454	3.6561	3.07×10^{-64}	200.64	199.68	38.504
1/100	0.0001	24.305	37.174	0.98524	2.5107	1.9367	0.010753
	0.001	10.698	16.491	0.93616	4.7349	3.7080	0.10044
	0.01	4.8457	7.3583	0.74503	9.8395	7.3743	0.85779
	0.1	2.9684	3.7386	0.22415	23.025	17.038	4.7124
	1	2.9097	2.9947	6.28×10^{-6}	28.819	27.146	6.6934
	10	2.9097	2.9182	2.02×10^{-51}	28.819	28.652	6.6935
1/10	0.0001	20.228	31.359	0.98753	1.3138	1.0024	0.0032024
	0.001	9.0448	13.946	0.94574	2.4934	1.9538	0.028218
	0.01	4.1029	6.2295	0.77944	4.4202	3.5519	0.21826
	0.1	2.4978	3.1550	0.28308	7.4799	6.1087	1.1599
	1	2.4490	2.5213	4.70×10^{-5}	9.0082	8.5635	1.7798
	10	2.4490	2.4562	2.14×10^{-43}	9.0084	8.9639	1.7799
1	0.0001	19.439	30.219	0.98798	1.1684	0.88977	0.0023736
	0.001	8.7209	13.453	0.94761	2.2373	1.7486	0.020300
	0.01	3.9621	6.0127	0.78623	3.8971	3.1627	0.14644
	0.1	2.4129	3.0470	0.29559	5.9224	5.0466	0.71083
	1	2.3666	2.4362	5.86×10^{-5}	6.8235	6.5517	1.0878
	10	2.3666	2.3736	5.85×10^{-42}	6.8237	6.7965	1.0879
10	0.0001	19.351	30.090	0.98804	1.1535	0.87823	0.0022891
	0.001	8.6846	13.398	0.94782	2.2113	1.7277	0.019494
	0.01	3.9465	5.9885	0.78699	3.8456	3.1239	0.13909
	0.1	2.4037	3.0351	0.29699	5.7674	4.9417	0.66377
	1	2.3576	2.4269	6.08×10^{-5}	6.6009	6.3477	1.0136
	10	2.3576	2.3646	8.38×10^{-42}	6.6011	6.5757	1.01373
∞	0.0001	19.341	30.076	0.98804	1.1519	0.87695	0.0022797
	0.001	8.6805	13.391	0.94784	2.2084	1.7254	0.019404
	0.01	3.9447	5.9858	0.78707	3.8398	3.1196	0.13827
	0.1	2.4027	3.0338	0.29715	5.7501	4.9300	0.65851
	1	2.3566	2.4259	6.11×10^{-5}	6.5761	6.3250	1.0053
	10	2.3566	2.3635	8.73×10^{-42}	6.5763	6.5511	1.0054

Table 6
Limiting dimensionless heat transfer quantities as $M\,Da \to 0$

2ϕ (°)	$\bar{x}$	Nu_D	$\overline{N}u_D$	$\theta_{b,I}$	$(M\,Da)q_w^*$	$(M\,Da)\bar{q}_w^*$	$(M\,Da)\theta_{b,S}$
30	0.0001	56.661	112.85	0.95586	0.0018657	0.0013154	1.6383×10^{-5}
	0.001	19.134	36.926	0.86269	0.0058046	0.0039080	1.5346×10^{-4}
	0.01	7.1327	12.669	0.60245	0.016806	0.011583	0.0012276
	0.1	4.2219	5.5369	0.10918	0.037658	0.028862	0.0053646
	1	4.1396	4.2826	3.63×10^{-8}	0.042273	0.040656	0.0064710
	10	4.1396	4.1539	6.92×10^{-73}	0.042273	0.042111	0.0064710
60	0.0001	57.203	111.78	0.95627	0.0048584	0.0034153	0.000043078
	0.001	19.091	36.977	0.86251	0.015276	0.010275	0.00040334
	0.01	7.1573	12.688	0.60198	0.044224	0.030470	0.0032256
	0.1	4.40350	5.6275	0.10529	0.099412	0.076106	0.014002
	1	4.3865	4.5109	1.46×10^{-8}	0.11111	0.10694	0.016667
	10	4.3865	4.3989	3.83×10^{-77}	0.11111	0.11069	0.016667
90	0.0001	56.659	112.12	0.95614	0.0075249	0.0053058	0.000066507
	0.001	19.114	36.965	0.86255	0.023582	0.015863	0.00062284
	0.01	7.1394	12.674	0.60231	0.068232	0.047023	0.0049820
	0.1	4.2807	5.5642	0.10799	0.15304	0.11725	0.021729
	1	4.2334	4.3678	2.58×10^{-8}	0.17157	0.16505	0.026090
	10	4.2334	4.2468	1.68×10^{-74}	0.17157	0.17092	0.026090

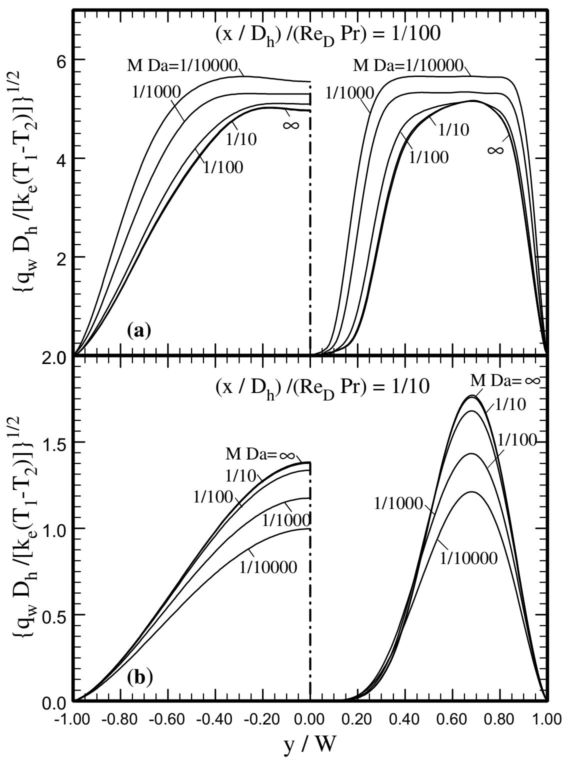

Fig. 6. Heat flux variation along $z = H$ and $z = Hy/W$ walls of the triangular passage in Fig. 2 with $2\phi = 30°$ due to wall temperature change, when (a) $\bar{x} = 0.01$ and (b) $\bar{x} = 0.1$.

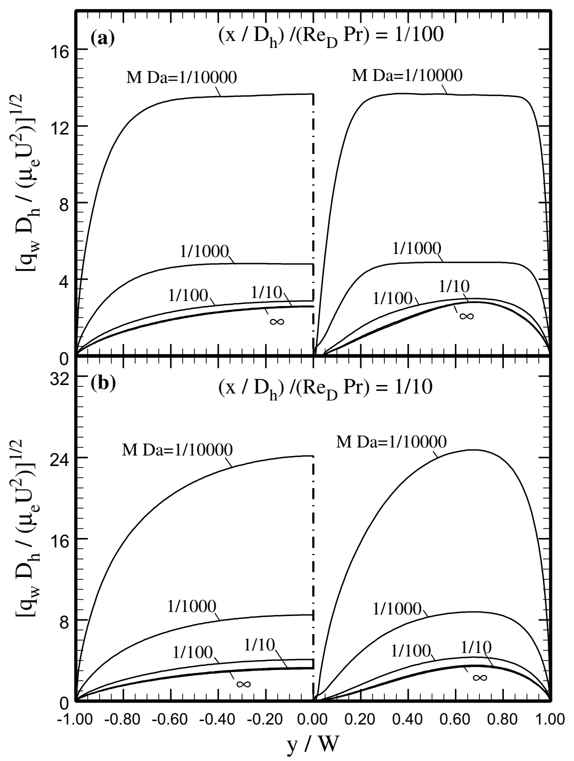

Fig. 7. Heat flux variation along $z = H$ and $z = Hy/W$ walls of the triangular passage in Fig. 2 with $2\phi = 30°$ due to frictional heating effects, when (a) $\bar{x} = 0.01$ and (b) $\bar{x} = 0.1$.

$$q_w = k\nabla T \cdot \vec{n} = \frac{k[-(\partial T/\partial y)H/W + (\partial T/\partial z)]}{(H/W)^2 + 1}. \tag{35}$$

The abscissa of Fig. 6 is the distance y/W and the ordinate is the dimensionless heat flux $q_w D_h/[k(T_2 - T_1)]$. The right side of Figs. 6–8 shows the heat flux along the $z = Hy/W$ surface and the left side is for the $z = H$ surface. The heat transfer data, tabulated in Tables 3–5 and plotted in Figs. 2–5, describe the effects of the circumferentially averaged heat flux. For example, the circumferentially averaged heat flux due to a temperature change at the wall, $q_w D_h/[k(T_2 - T_1)$, is the product of

$Nu_D \theta_{b,i} = (hD_h/k_e)[(T_b - T_2)/(T_1 - T_2)]$

since $q_w = h(T_2 - T_b)$. Fig. 6 demonstrates the local wall heat flux plotted along the perimeter of the triangular passage; $(x/D_h)/(Re_D Pr)$ is 0.01 for data in Fig. 6(a) and it is 0.1 for those in 6(b). The graph shows an onset of a cross-over, which is a remarkable feature. When $MDa = 1/10{,}000$, the data in Fig. 6(a) are the highest whereas in Fig. 6(b) those for $MDa = \infty$ have the highest values. As expected, the wall heat flux vector at the corners vanishes since it has zero components in two different directions. Also, the data in Table 3 show that $\theta_{b,i}$ becomes negligible when $\bar{x} = 1$ and this is in contrast to

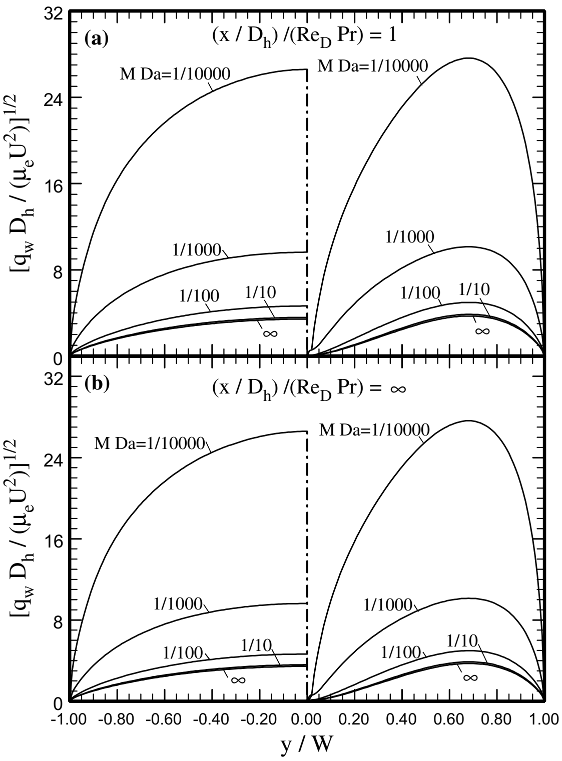

Fig. 8. Heat flux variation along $z = H$ and $z = Hy/W$ walls of the triangular passage in Fig. 2 with $2\phi = 30°$ due to frictional heating effects, when (a) $\bar{x} = 1$ and (b) $\bar{x} = \infty$.

the effect of the frictional heating. The local values of $[q_w D_h/(\mu_e U^2)]^{1/2}$ along the circumference of the passage are plotted in Fig. 7(a) and (b) when $\bar{x} = 0.01$ and 0.1. The data are relatively well behaved and they show significant variations as $(x/D_h)/(Re_D Pr)$ and MDa changes. The fully developed values of the local heat flux are plotted in Fig. 8(b). For comparison, similar data, when $\bar{x} = 1$, are plotted in Fig. 8(a). These last two sets indicate that changes in the value of local heat flux become small when $\bar{x} > 1$.

Often, it is customary to assume the wall temperature change to begin at $x = 0$ while fluid enters a pipe at $x = -\infty$. To meet this condition, the transformation of the dimensionless axial coordinate, as appeared earlier, considers an axial coordinate $x - x_0$ where the wall temperature changes. This permits the inclusion of the frictional heating effects when $x_0 \to \infty$. Accordingly, one can use the knowledge of heat transfer coefficient in the absence of frictional heating to compute the effect of wall temperature change at any location $\bar{x} = [(x - x_0)/D_h]/(Re_D Pr)$. Then, one can include the contribution of the frictional heating for any x_0 by viewing $\bar{x}$ in column 2 of Tables 3–5 to be $\bar{x} + \bar{x}_0$. These combined effects provide a desirable flexibility and will simplify the presentation of data as it reduces the needed parameters for each case. A proper combination of these two contributions yields the value of bulk temperature. As an illustration, using $\theta_{b,W} = (T_{b,W} - T_1)/(T_2 - T_1) = 1 - \theta_{b,I}$ and $\theta_{b,S} = [(T_{b,S} - T_1)/(T_2 - T_1)]/(PrEc)$, one can determine the bulk temperature from the relation

$$T_b - T_1 = (T_{b,S} - T_1) + (T_{b,W} - T_1). \tag{36}$$

Also, the combined effect of frictional heating and wall temperature change to the local wall heat flux is

$$q_w = q_{w,S} + q_{w,I} \tag{37}$$

and it includes the circumferentially averaged wall heat flux. Finally, the average wall heat flux is

$$\bar{q}_w = \bar{q}_{w,S} + \bar{q}_{w,I}. \tag{38}$$

6. Boundary conditions of the second kind

The methodology presented here is applicable to the case when the boundary condition is of the second or third kind. All computational steps leading to the Green's function solution, Eq. (22), remain the same except for the selection of the basis function. As an example, Beck et al. [3, Chapter 11] describes a procedure for finding the basis functions when one surface is having a boundary condition of the second kind. Therefore, for the boundary conditions of the second kind, this method provides:

Table 7
Computed heat transfer to fluid flow in parallel-plate channels and circular pipes with constant wall heat flux

$\frac{(x/D_h)}{Re_D Pr}$	Parallel-plate channels			Circular pipes		
	$M\,Da$, (S^*)	Nu_D	$\theta_{w,S}-\theta_{b,S}$	$M\,Da$, (S^*)	Nu_D	$\theta_{w,S}-\theta_{b,S}$
10^{-5}	∞ (3)	69.08	0.0170	∞ (8)	59.62	0.0101
5×10^{-5}		40.42	0.0472		34.49	0.0285
10^{-4}		32.16	0.0725		27.27	0.0442
5×10^{-4}		19.11	0.1875		15.81	0.1192
10^{-3}		15.43	0.2739		12.54	0.1794
5×10^{-3}		9.988	0.5713		7.494	0.4288
10^{-2}		8.803	0.6973		6.148	0.5907
5×10^{-2}		8.236	0.7714		4.514	0.9516
10^{-1}		8.235	0.7714		4.375	0.9963
∞		8.235	0.7714		4.364	1.000
10^{-5}	10^{-1} (14.601)	78.92	0.0268	10^{-1} (20.809)	66.03	0.0142
5×10^{-5}		45.96	0.0691		37.98	0.0386
10^{-4}		36.44	0.1013		29.98	0.0585
5×10^{-4}		21.43	0.2273		17.32	0.1456
10^{-3}		17.20	0.3072		13.72	0.2093
5×10^{-3}		10.94	0.5326		8.170	0.4368
10^{-2}		9.560	0.6183		6.698	0.5636
5×10^{-2}		8.862	0.6715		4.934	0.8110
10^{-1}		8.861	0.6716		4.793	0.8383
∞		8.861	0.6716		4.783	0.8403
10^{-5}	10^{-2} (111.11)	103.9	0.0684	10^{-2} (123.41)	83.31	0.0342
5×10^{-5}		59.85	0.1504		48.35	0.0839
10^{-4}		47.12	0.2012		38.12	0.1194
5×10^{-4}		27.09	0.3426		21.86	0.2433
10^{-3}		21.46	0.4030		17.23	0.3122
5×10^{-3}		13.15	0.5112		10.16	0.4770
10^{-2}		11.28	0.5407		8.298	0.5358
5×10^{-2}		10.26	0.5601		6.142	0.6164
10^{-1}		10.26	0.5601		5.994	0.6231
∞		10.26	0.5601		5.986	0.6235
10^{-5}	10^{-3} (1032.7)	143.9	0.1787	10^{-3} (1066.4)	114.1	0.1004
5×10^{-5}		80.34	0.3015		66.48	0.2012
10^{-4}		62.28	0.3531		51.68	0.2562
5×10^{-4}		34.12	0.4446		28.82	0.3840
10^{-3}		26.34	0.4698		22.38	0.4291
5×10^{-3}		15.17	0.5046		12.65	0.4987
10^{-2}		12.72	0.5128		10.16	0.5159
5×10^{-2}		11.32	0.5186		7.333	0.5361
10^{-1}		11.32	0.5186		7.151	0.5377
∞		11.32	0.5186		7.141	0.5378
10^{-5}	10^{-4} (10101)	193.0	0.3373	10^{-4} (10203)	158.3	0.2446
5×10^{-5}		102.2	0.4244		88.52	0.3563
10^{-4}		76.96	0.4483		67.58	0.3977
5×10^{-4}		39.29	0.4812		35.54	0.4614
10^{-3}		29.51	0.4891		26.83	0.4773
5×10^{-3}		16.17	0.4996		14.28	0.4987
10^{-2}		13.37	0.5021		11.24	0.5036
5×10^{-2}		11.77	0.5039		7.917	0.5094
10^{-1}		11.77	0.5039		7.708	0.5098
∞		11.77	0.5039		7.697	0.5099

1. For flow between two parallel plates with walls located at $y = \pm H$, the basis functions are
$$f_j = \{(j-1)[1-(y/H)^2]+1\}(y/H)^{2(j-1)}$$
with $j = 1, 2, \ldots, N$.

2. For a circular pipe with radius r_0, the basis functions are similar,
$$f_j = \{(j-1)[1-(r/r_0)^2]+1\}(r/r_0)^{2(j-1)}$$
with $j = 1, 2, \ldots, N$.

3. For an elliptical passage with the wall being at $(y/a)^2 + (z/b)^2 = 1$, the basis functions are
$$\left\{\frac{[b^2(m_j-1)+a^2(n_j-1)][1-(y/a)^2-(z/b)^2]}{a^2-y^2(1-b^2/a^2)}-1\right\} \times y^{2(m_j-1)}z^{2(n_j-1)},$$
when using all combinations of m_j and n_j.

Indeed, this method provides the following basis functions for a rectangular passage with walls located at $y = \pm a$ and $z = \pm b$,
$$f_j = \left[1+(m_j-1)(1-y^2/a^2)\right] \times \left[1+(n_j-1)(1-z^2/b^2)\right]y^{2(m_j-1)}z^{2(n_j-1)},$$
when all surfaces of a rectangle have the boundary condition of the second kind. Also, a similar procedure but with a minor modification is available in [3, p. 345] if these boundary conditions are of the third kind. Although all these basis functions were tested and they performed well, only sample data are to appear next. For triangular passages, the method in [3] can define a set of basis functions when the heat flux is prescribed on one side of a triangular passage and there will be different sets depending on the location of the boundary condition of the second kind.

The Nusselt number values are computed, for flow through parallel-plate channels and for circular pipes, by modifying the procedure presented in Example 1. A single program written in Mathematica [13] performed this task. The local Nusselt number values in the absence of frictional heating are obtained at different $(x/D_h)/(Re_D Pr)$ and for different MDa values. The data in Column 3 of Table 7 are for parallel-plate channels and those in Column 6 are for circular pipes. The computed values are in general agreement with those reported in [9]. When heat flux is prescribed, the average wall heat flux $\bar{q}_w$, at any location x, is related to the bulk temperature by the relation $\bar{q}_{w,W}Cx = \rho UAc_p(T_{b,W} - T_1)$ that becomes $\theta_{b,W} = 4\bar{x}\bar{q}^*_{w,W}$; for the case of constant wall heat flux, $\bar{q}^*_w = q^*_w$. Once θ_b is known, the definition of heat transfer coefficient, $q_{w,W} = h(T_{w,W} - T_{b,W})$, leads to the relation $\theta_{w,W} = \theta_{b,W} + 4q^*_{w,W}/Nu_D$ while both $\theta_{b,W}$ and Nu_D depend on $\bar{x}$.

In the computation of the contribution of frictional heating, it is hypothesized that $q_{w,S} = 0$ everywhere along the channel. The only quantity that remains to be determined is $T_{w,S}$ and, in the dimensionless form, it becomes $\theta_{w,S} = k_e(T_{w,S} - T_1)/(\mu_e U^2)$. Table 7 contains the values $\theta_{w,S} - \theta_{b,S}$ tabulated at different $(x/D_h)/(Re_D Pr)$ and MDa values. The tabulated data show that, for each MDa, this quantity approaches a constant value as x increases. These values of $\theta_{w,S}$ are deterministic since $\theta_{b,S} = S^*(x/D_h)/(Re_D Pr)$ and S^*, in Eq. (27b), depend only on MDa. The numerical value of each S^* is within parentheses in Columns 2 and 5 of Table 7 listed after the corresponding MDa value and they are accurate to all digits listed for larger MDa and $\bar{x}$ values. The data show that the value of $\theta_{w,S} - \theta_{b,S}$ becomes negligible in comparison with S^* as MDa decreases.

7. Conclusion

For flow through porous passages, the hydrodynamic entrance region is expected to be small. This causes the velocity profile to quickly reach the fully developed condition and, therefore, the governing momentum equation becomes linear. This presentation demonstrated that the Green's function solution method is a powerful tool to accommodate many aspects of the heat transfer problems associated with flow through porous passages. The capability of this solution is enhanced when the Green's function is computed by extending the method of weighted residuals. The numerical data attest that solutions with a high degree of accuracy are attainable with relative ease. Furthermore, this methodology is applicable to various other heat transfer problems when the energy equation is linear. An example is its application to laminar MHD flow through a parallel-plate channel [16].

References

[1] E.M. Sparrow, R. Seigel, A variational method for fully developed laminar heat transfer in ducts, J. Heat Transfer, Trans. ASME 81 (2) (1959) 157–167.
[2] L.V. Kantorovich, V.I. Krylov, Approximate Methods of Higher Analysis, Wiley, New York, 1960.
[3] J.V. Beck, K.D. Cole, A. Haji-Sheikh, B. Litkouhi, Heat Conduction Using Green's Functions, Hemisphere Publ. Corp., Washington, DC, 1992.
[4] A. Haji-Sheikh, K. Vafai, Analysis of flow and heat transfer in porous media imbedded inside various-shaped ducts, Int. J. Heat Mass Transfer 47 (8–9) (2004) 1889–1905.
[5] A. Haji-Sheikh, W.J. Minkowycz, E.M. Sparrow, Green's function solution of temperature field for flow in porous passages, Int. J. Heat Mass Transfer 47 (22) (2004) 4685–4695.
[6] D.A. Nield, A.V. Kuznetsov, M. Xiong, Thermally developing forced convection in a porous medium: parallel plate

channel with walls at uniform temperature, with axial conduction and viscous dissipation effects, Int. J. Heat Mass Transfer 46 (4) (2003) 643–651.
[7] A.V. Kuznetsov, D.A. Nield, M. Xiong, Thermally developing forced convection in a porous medium: circular ducts with walls at constant temperature, with longitudinal conduction and viscous dissipation effects, Transp. Porous Media 53 (3) (2003) 331–345.
[8] A.K. Al-Hadhrami, L. Elliot, D.B. Ingham, A new model for viscous dissipation in porous media across a range of permeability values, Transp. Porous Media 53 (1) (2003) 117–122.
[9] D.A. Nield, A.V. Kuznetsov, M. Xiong, Thermally developing forced convection in a porous medium: parallel-plate channel or circular tube with walls at constant heat flux, J. Porous Media 6 (3) (2003) 203–212.
[10] K. Vafai (Ed.), Handbook of Porous Media, Marcel Dekker, New York, 2000.
[11] D.A. Nield, A. Bejan, Convection in Porous Media, second ed., Springer-Verlag, New York, 1999.
[12] K. Kaviany, Principles of Heat Transfer in Porous Media, Springer-Verlag, New York, 1991.
[13] S. Wolfram, The Mathematica Book, fourth ed., Cambridge University Press, Cambridge, UK, 1999.
[14] A. Haji-Sheikh, W.J. Minkowycz, E.M. Sparrow, A numerical study of the heat transfer to fluid flow through circular porous passages, Numer. Heat Transfer, Part A 46 (10) (2004) 929–956.
[15] R. Lakshminarayanan, A. Haji-Sheikh, Entrance heat transfer in isosceles and right triangular ducts, AIAA J. Thermophys. Heat Transfer 6 (1) (1992) 167–171.
[16] J. Lahjomri, A. Oubarra, A. Alemany, Heat transfer by laminar Hartmann flow in thermal entrance region with a step change in wall temperature: the Graetz problem extended, Int. J. Heat Mass Transfer 45 (5) (2002) 1127–1148.